Nanoscale Advances

ROYAL SOCIETY OF CHEMISTRY

PAPER

View Article Online
View Journal | View Issue

Cite this: *Nanoscale Adv.*, 2024, **6**, 3410

Multiscale modeling of surface enhanced fluorescence†

Pablo Grobas Illobre, Piero Lafiosca, Teresa Guidone, Francesco Mazza, Tommaso Giovannini * and Chiara Cappelli *

Received 26th January 2024
Accepted 20th May 2024

DOI: 10.1039/d4na00080c

rsc.li/nanoscale-advances

The fluorescence response of a chromophore in the proximity of a plasmonic nanostructure can be enhanced by several orders of magnitude, yielding the so-called surface-enhanced fluorescence (SEF). An in-depth understanding of SEF mechanisms benefits from fully atomistic theoretical models because SEF signals can be non-trivially affected by the atomistic profile of the nanostructure's surface. This work presents the first fully atomistic multiscale approach to SEF, capable of describing realistic structures. The method is based on coupling density functional theory (DFT) with state-of-the-art atomistic electromagnetic approaches, allowing for reliable physically-based modeling of molecule–nanostructure interactions. Computed results remarkably demonstrate the key role of the NP morphology and atomistic features in quenching/enhancing the fluorescence signal.

1 Introduction

Under the action of an external electric field, metal nanoparticles (NPs) can exhibit localized surface plasmons (LSPs), which are collective excitations of conductive electrons. LSPs are associated with a significant enhancement of the induced electric field, up to several orders of magnitude. When a molecular system is posed in the NP proximity, its photophysical and spectral properties can be substantially affected, yielding the so-called surface-enhanced spectroscopies.[1–15] Among them, Surface-Enhanced Fluorescence (SEF) exploits the enhancement of the fluorescence signal, which can be useful to study biological matrices interacting with plasmonic nanostructures for biosensing applications.[16–20] Remarkably, precise control of the NP structure and the resulting plasmonic response has enabled the mapping of single molecules, achieving submolecular resolution, within the so-called Tip-Enhanced Photoluminescence (TEPL) experiments.[21–24] The interplay of the complex physical phenomena underlying SEF and related techniques, such as the optical response of plasmonic substrates and their interaction with the electronic structure of the chromophore, are still not fully understood, thus challenging the rationalization of the measured results. In this context, reliable computational approaches capable of accurately describing how the NP structure affects SEF signals are needed, especially those models featuring a fully atomistic, realistic description of the nanosystem.[18,22,25–30]

In this work, the first fully atomistic multiscale approach to SEF is developed. The model can be used to describe realistic nanostructures with atomistic details, substantially overcoming common issues related to the huge computational cost of full QM treatments of the system, which only allows the description of systems (molecule + nanostructure) composed of a few atoms.[28,31,32] Our approach is based on the coupling of quantum mechanics (QM), defined at the density functional theory (DFT) level to determine the molecular electronic structure, with a novel fully atomistic electrodynamical approach to describe the plasmonic response of complex-shaped nanostructures, namely the frequency-dependent fluctuating charges and fluctuating dipoles (ωFQFμ) method.[33,34] ωFQFμ is physically grounded on the Drude conduction model, electrostatics, and interband transitions and includes corrections to describe quantum tunneling effects, which can be crucial to reliably model nanoaggregates. In ωFQFμ, each metal atom is endowed with a fluctuating charge, accounting for intraband transitions (Drude regime), and a fluctuating dipole, describing interband transitions. The method can remarkably capture plasmonic properties of systems featuring subnanometer junctions[35–37] and defects.[38–40] Recent extensions have also permitted the calculation of the plasmonic response of bimetallic systems.[41] Notably, ωFQFμ reproduces *ab initio* results, questioning the common notion that an explicit QM treatment is needed for describing plasmonic response upon shrinking the nanostructure size.[33] Furthermore, the coupling of ωFQFμ to a QM formalism (QM/ωFQFμ) to evaluate surface-enhanced Raman scattering (SERS) signals of molecules in the vicinity of complex-shaped nanostructures, has recently been proposed.[34]

Scuola Normale Superiore, Piazza dei Cavalieri 7, 56126 Pisa, Italy. E-mail: tommaso.giovannini@sns.it; chiara.cappelli@sns.it

† Electronic supplementary information (ESI) available: Details on the BEM model. Geometrical parameters and computed plasmon resonance frequencies. Atomistic *vs.* Continuum for Ag structures. Fluorescence Dependence on NP size and morphology. PDI interacting with Ag Nanorods. PDI interacting with NP dimers. See DOI: https://doi.org/10.1039/d4na00080c

In this paper, QM/ωFQFμ is extended to the calculation of SEF signals. The modeling of fluorescence processes presents significant challenges compared to SERS. Specifically, the electronic structure of both the molecular Ground State (GS) and the emitting Excited State (ES) needs to be accurately described. This is achieved in terms of a Time-Dependent Density Functional Theory (TD-DFT)/ωFQFμ formalism, which is specified by reformulating at the fully atomistic level the methodology proposed for implicit, non-atomistic, descriptions of the nanostructure.[27–29,42–45] The latter describe the nanostructure as a continuum dielectric whose response is determined by the permittivity functions. Due to their implicit nature, atomistic features and their effect on the molecular response are neglected.

The manuscript is organized as follows. In Section 2, the theoretical foundations of ωFQFμ are recalled, and its coupling to a TDDFT formalism to study the SEF response is presented. After highlighting the computational details, in Section 4, TDDFT/ωFQFμ is challenged to simulate SEF of a well-studied chromophore (*N*,*N*′-dimethylperylene 3,4,9,10-dicarboximide – PDI) near metal NPs of increasing complexity. Conclusions and future perspectives end the manuscript.

2 Theory

2.1 ωFQFμ

ωFQFμ is a fully atomistic model specifically developed for studying plasmonic responses of metal NPs.[33,35] It combines the Drude model for intraband transitions with an effective polarizability, which mimics core electrons and interband transitions.[46–49] To physically consistently model both mechanisms, each atom is endowed with a charge (ωFQ) and a dipole (ωFμ). Under the action of a monochromatic external electric field, the atoms exchange charge *via* the Drude conduction mechanism, which is further assisted by quantum tunneling, thus limiting charge transfer among the nearest neighboring atoms and making the interaction decrease with the typical exponential decay. In particular, ωFQ charge equation of motion in the frequency domain (ω) reads:[33,35,37]

$$-i\omega q_i(\omega) = \frac{2n_0\tau}{1-i\omega\tau}\sum_j \left[1-f\left(r_{ij}\right)\right]\frac{\mathcal{A}_{ij}}{r_{ij}}\left(\phi_j^{\mathrm{el}}-\phi_i^{\mathrm{el}}\right) \quad (1)$$

where q_i is the electric charge on the i-th atom, n_0 is the 3D density, τ the scattering time, and $\mathcal{A}_{ij}$ denotes the effective area connecting atoms i and j. The Fermi damping function $f(r_{ij})$ describes quantum tunneling effects[35] in terms of the interatomic distance $r_{ij} = |r_i - r_j|$ (r_i is the position of atom i). ϕ_i^{el} accounts for the electrochemical potential of the i-th atom, and takes into account charge–charge and charge–dipole interactions, and the external electric field.

To introduce interband effects, each atom is assigned an additional source of polarization, *i.e.*, atomic polarizability, to which an induced dipole moment is associated. The induced dipole moments μ_i are obtained by solving the following linear equation:[33]

$$\mu_i = \alpha_i^{\omega}(\mathbf{E}_i^{\mathrm{ext}} + \mathbf{E}_i^{\mu} + \mathbf{E}_i^{\mathrm{q}}) \quad (2)$$

where $\mathbf{E}_i^{\mathrm{ext}}$, $\mathbf{E}_i^{\mu}$ and $\mathbf{E}_i^{\mathrm{q}}$ are the external electric field and the electric fields on atom i generated by the other dipoles and charges, respectively. Additionally, α_i^{ω} is the atomic complex polarizability, which mimics interband transitions.[33,41] Remarkably, α_i^{ω} can be easily obtained by extracting interband contributions from the experimental permittivity function without introducing *a posteriori* any adjustable parameters.[33,41]

To effectively couple charges and dipoles, eqn (1) and (2) are simultaneously solved using the following set of linear equations:[33]

$$\left[\begin{pmatrix}\mathbf{D}^{\mathrm{q}} & \mathbf{D}^{\mathrm{q}\mu}\\ \mathbf{T}^{\mu\mathrm{q}} & \mathbf{T}^{\mu\mu}\end{pmatrix} - \begin{pmatrix} z(\omega)\mathbf{I}_N & 0\\ 0 & z'(\omega)\mathbf{I}_{3N}\end{pmatrix}\right]\begin{pmatrix}\mathbf{q}\\ \boldsymbol{\mu}\end{pmatrix} = \begin{pmatrix}\mathbf{R}\\ -\mathbf{E}^{\mathrm{ext}}\end{pmatrix} \quad (3)$$

where $\mathbf{D}^{\mathrm{q}}$ gathers the interaction between charges, $\mathbf{D}^{\mathrm{q}\mu}$ accounts for the charge–dipole terms, and $\mathbf{T}^{\{\{\mu\}\mathrm{q}\}}$ and $\mathbf{T}^{\mu\mu}$ matrices represent the charge–dipole and dipole–dipole interaction kernels, respectively.[50] $\mathbf{I}_N$ is the $N \times N$ identity matrix, where N is the number of atoms. z and z' functions are the complex frequency-dependent diagonal shifts associated with charges and dipoles, respectively (see ref. 33 for their definitions). In the right-hand side, $\mathbf{R}$ and $\mathbf{E}^{\mathrm{ext}}$ enclose the effect of the external potential and field acting on each charge and dipole.

2.2 QM/classical coupling (QM/ωFQFμ) and fluorescence descriptors

To evaluate the fluorescence response of a chromophore when it is influenced by the plasmonic response of a nearby metallic NP, ωFQFμ is coupled with a QM treatment of the molecule, in a multiscale fashion. Through the developed method, the effect of NP atomistic features on the fluorescence response of the nearby molecular system is evaluated, thus overcoming the limitations of QM/continuum methodologies previously proposed.[27–29,42,43,45]

Molecular fluorescence response originates from the following subsequent processes: (a) initially, the molecule absorbs a photon from the incident electric field, being promoted to an ES; (b) the molecule undergoes internal relaxation, reaching the minimum of the emitting ES; (c) the chromophore decays to the GS, either radiatively, emitting a photon, or non-radiatively.[27–29,43,45]

We exploit the time-dependent formulation of density functional theory (TD-DFT)[42,44,51] and we modify it to take into account the effects of the plasmonic NP. Within a QM/ωFQFμ formalism, Casida's equations read:[34]

$$\left[\begin{pmatrix}\mathbf{A}(\omega) & \mathbf{B}(\omega)\\ \mathbf{B}^*(-\omega^*) & \mathbf{A}^*(-\omega^*)\end{pmatrix} - \omega\begin{pmatrix}\mathbf{I} & 0\\ 0 & -\mathbf{I}\end{pmatrix}\right]\begin{pmatrix}\mathbf{X}_\omega\\ \mathbf{Y}_\omega\end{pmatrix} = 0 \quad (4)$$

$$A_{\mathrm{ai,bj}}(\omega) = (\varepsilon_{\mathrm{a}} - \varepsilon_{\mathrm{i}})\delta_{\mathrm{ab}}\delta_{\mathrm{ij}} + K^0_{\mathrm{ai,bj}} + K^{\mathrm{pol}}_{\mathrm{ai,bj}}(\omega) \quad (5a)$$

$$B_{\mathrm{ai,bj}}(\omega) = K^0_{\mathrm{ai,jb}} + K^{\mathrm{pol}}_{\mathrm{ai,jb}}(\omega) \quad (5b)$$

where ω is the excitation frequency while $\mathbf{X}_\omega$ and $\mathbf{Y}_\omega$ are the excitation and de-excitation transition densities, respectively. Eqn (4) contains **AB** TD-DFT matrices defined in eqn (5a) and

(5b), whose elements (i, j/a, b indices run over occupied/virtual orbitals) are defined in terms of the molecular orbital energies ε. $K^{0}_{\mathrm{ai,bj}}$ is the exchange-correlation contribution, while $\mathbf{K}^{\mathrm{pol}}$ is a frequency-dependent term that includes the polarization arising from the NP, which is expressed as:

$$K^{\mathrm{pol}}_{\mathrm{ai,bj}}(\omega) = \sum_{\nu} \mathbf{q}(\omega)\left(r_{\nu}, \left[\mathbf{\Psi}^{*}_{\mathrm{a}}\mathbf{\Psi}_{\mathrm{i}}\right]\right)\mathbf{V}\left(r_{\mathrm{v}}, \left[\mathbf{\Psi}^{*}_{\mathrm{b}}\mathbf{\Psi}_{\mathrm{j}}\right]\right) - \sum_{\nu} \boldsymbol{\mu}(\omega)\left(r_{\nu}, \left[\mathbf{\Psi}^{*}_{\mathrm{a}}\mathbf{\Psi}_{\mathrm{i}}\right]\right)\mathbf{E}\left(r_{\mathrm{v}}, \left[\mathbf{\Psi}^{*}_{\mathrm{b}}\mathbf{\Psi}_{\mathrm{j}}\right]\right) \tag{6}$$

where $\mathbf{q}(\omega)(r_{\nu}, [\mathbf{\Psi}^{*}_{\mathrm{a}}\mathbf{\Psi}_{\mathrm{i}}])$ and $\boldsymbol{\mu}(\omega)(r_{\nu}, [\mathbf{\Psi}^{*}_{\mathrm{a}}\mathbf{\Psi}_{\mathrm{i}}])$ represent the frequency-dependent charges and dipoles at the atomic position r_{ν}, induced by the $\mathbf{\Psi}^{*}_{\mathrm{a}}\mathbf{\Psi}_{\mathrm{i}}$ distribution. They interact with the potential $\mathbf{V}(r_{\nu}, [\mathbf{\Psi}^{*}_{\mathrm{j}}\mathbf{\Psi}_{\mathrm{b}}])$ and field $\mathbf{E}(r_{\nu}, [\mathbf{\Psi}^{*}_{\mathrm{j}}\mathbf{\Psi}_{\mathrm{b}}])$ generated by the $\mathbf{\Psi}^{*}_{\mathrm{j}}\mathbf{\Psi}_{\mathrm{b}}$ distribution, respectively.

From the mathematical point of view, $\mathbf{q}$ and $\boldsymbol{\mu}$ are complex quantities, making $\mathbf{K}^{\mathrm{pol}}$ complex. By following ref. 42, the modified TD-DFT problem is solved by treating the imaginary parts as a perturbation to the first order. In particular, excitation energies and transition densities are computed from the real part of the poles (eqn (4)) as follows ($'$ indicates real quantities):[42]

$$\left[\begin{pmatrix} \mathbf{A}'(\omega') & \mathbf{B}'(\omega') \\ \mathbf{B}'(-\omega') & \mathbf{A}'(-\omega') \end{pmatrix} - \omega' \begin{pmatrix} \mathbf{I} & 0 \\ 0 & -\mathbf{I} \end{pmatrix}\right]\begin{pmatrix} \mathbf{X}'_{\omega} \\ \mathbf{Y}'_{\omega} \end{pmatrix} = 0 \tag{7}$$

The imaginary excitation frequency can be computed by exploiting the perturbative treatment as: ($''$ marks imaginary parts):[42]

$$\omega'' = \left[\begin{pmatrix} \mathbf{X}'^{\dagger}_{\omega} & \mathbf{Y}'^{\dagger}_{\omega} \end{pmatrix}\begin{pmatrix} \mathbf{A}''(\omega') & \mathbf{B}''(\omega') \\ -\mathbf{B}''(-\omega') & -\mathbf{A}''(-\omega') \end{pmatrix}\begin{pmatrix} \mathbf{X}'_{\omega} \\ \mathbf{Y}'_{\omega} \end{pmatrix}\right] \tag{8}$$

The response imaginary component is associated with the molecular non-radiative lifetime (τ^{nr}) through the inverse of the non-radiative decay rate (Γ^{nr}). The latter is given by:[44]

$$\Gamma^{\mathrm{nr}} = \frac{1}{\tau^{\mathrm{nr}}} = -2\omega_{\mathrm{Im}} \tag{9}$$

The molecular radiative energy dissipation instead generates the fluorescence signal from the emitting ES to GS. This is generally characterized by the radiative lifetime (τ^{r}), which can be expressed as the inverse of the radiative decay rate (Γ^{r}). Furthermore, the emission probability is defined by the absorption coefficient (A), which is related to the population of the emitting ES. Within QM/ωFQFμ, A and Γ^{r} are calculated (in a. u.) as follows:

$$A = \frac{2\pi}{3c}\left|\mathbf{d}^{0\mathrm{K}}_{\mathrm{tot}}\right|^{2} \tag{10}$$

$$\Gamma^{\mathrm{r}} = \frac{4\omega'^{3}}{3c^{3}}\left|\mathbf{d}^{\mathrm{K0}}_{\mathrm{tot}}\right|^{2} \tag{11}$$

where c is the speed of light, whereas $\mathbf{d}^{0\mathrm{K}}_{\mathrm{tot}}$ is the total transition dipole from the molecular GS to the K-th ES. This takes into account both the molecular transition dipole moment ($\mathbf{d}^{\mathrm{K0}}_{\mathrm{mol}}$, calculated by solving eqn (7)) and the dipole moment induced on the plasmonic NP by the molecular transition ($\mathbf{d}^{\mathrm{K0}}_{\mathrm{plas}}$).[29] Thus, they can be defined as:

$$\mathbf{d}^{\mathrm{K0}}_{\mathrm{tot}} = \mathbf{d}^{\mathrm{K0}}_{\mathrm{mol}} + \mathbf{d}^{\mathrm{K0}}_{\mathrm{plas}} \tag{12}$$

$$\mathbf{d}^{\mathrm{K0}}_{\mathrm{plas}} = \sum_{i} q^{\mathrm{K0}}_{i}\mathbf{r}_{i} + \sum_{i} \mu^{\mathrm{K0}}_{i} \tag{13}$$

where q^{K0} and μ^{K0} are ωFQFμ charges and dipoles induced by the molecular transition $0 \rightarrow \mathrm{K}$. As stated above, the efficiency of fluorescence response arises from the interplay of the discussed processes. To account for both the absorption and emission mechanisms, the relative brightness (Φ^{RB}) is computed in the following way:

$$\Phi^{\mathrm{RB}} = \frac{A}{A^{\mathrm{free}}}\left(\frac{\Gamma^{\mathrm{r}}}{\Gamma^{\mathrm{r}} + \Gamma^{\mathrm{nr}}}\right) = \frac{A}{A^{\mathrm{free}}}\Phi^{\mathrm{FQY}} \tag{14}$$

where A/A^{free} is the absorption ratio in the presence or absence of the NP. The absorption ratio is multiplied by the number of emitted photons against the total number of absorbed photons. Such ratio is generally called fluorescence quantum yield (Φ^{FQY}), which is lower or equal to one by definition. Φ^{RB} quantifies fluorescence enhancement or quenching of the chromophore signal as a result of the interaction with the plasmonic NP.[27–29]

3 Computational details

The method is applied to studying the fluorescence response of *N*,*N*′-dimethylperylene 3,4,9,10-dicarboximide (PDI) chromophore as interacting with metal nanostructures of different shapes and dimensions. Both a longitudinal (L) and transversal (T) orientation of PDI relative to the NPs are considered. The fluorescence response is then investigated as a function of the PDI-NP distance (from 3 to 200 Å compared to the closest PDI hydrogen atom). In all calculations, PDI is treated at the QM level, while the metal nanostructure is classically described by using ωFQFμ. The latter is compared to the implicit description of the plasmonic systems to validate the novel approach, as provided by the BEM method. Following ref. 27, the NP response is computed at the experimental absorption (515 nm) and emission (525 nm) frequencies of PDI dissolved in *n*-heptane. The absorption coefficient (eqn (10)) is computed from the GS optimized geometry of PDI, while the non radiative decay and radiative decay rates (eqn (9) and (11)) are evaluated using the first ES optimized geometry.

Atomistic NPs are built with the Atomic Simulation Environment (ASE) Python module v. 3.17.[52] A face-centered cubic (FCC) arrangement and a lattice parameter of 4.08 Å are exploited, for both Ag and Au NPs. The geometrical relaxation of NPs is not considered because it slightly affects their optical response, as reported in ref. 33.[53–59] Four morphologies are analyzed: spherical, cuboctahedral (cTO), icosahedral (Ih), and cylindrical rods. The optical response of such NPs is simulated

employing ωFQFμ, using the parameters reported in ref. 33 (see also Table S3 in the ESI†). ωFQFμ charges and dipoles are calculated by solving eqn (3) by direct matrix inversion for the single rods and spherical, Ih, and cTO structures with radius ≤30 Å. For all other studied systems (Tables S1 and S2 of the ESI†), the Generalized Minimal RESidual method (GMRES) is used (RMSD threshold $= 1.0 \times 10^{-11}$).[37]

Spherical continuum structures are created using GMSH code,[60] with 5890 tesserae for each NP. Their optical properties are studied at the BEM level, using the Dielectric Polarizable Continuum Model (DPCM) formalism (see Sec. S1.1 of the ESI† for more details).[61–63] For both Ag and Au NPs, the frequency-dependent permittivity function of Etchegoin *et al.*[64] as fitted by Johnson and Christy[65,66] is used. The permittivity function is corrected to account for the dependence of the mean free path of the electrons on the sphere radius, as described in ref. 27. BEM equations are solved by matrix inversion (see eqn (1) of the ESI†). More details about the geometries and the associated Plasmon Resonance Frequencies (PRFs) are given in Tables S1 and S2 in the ESI.†

In all calculations, the PDI is described at the (TD-) DFT level by using the B3LYP functional combined with a double-ζ-polarized DZP basis set.[27] All QM/ωFQFμ and QM/BEM calculations are performed by using a locally modified version of the Amsterdam Modelling Suite (AMS).[67]

4 Results and discussion

In this section, ωFQFμ is applied to compute the fluorescence response of PDI placed near noble metal NPs. First, QM/ωFQFμ and QM/BEM implementations are validated on spherical NPs. Then, QM/ωFQFμ is used to investigate the effect of different geometrical arrangements/parameters on the PDI fluorescence response.

4.1 Atomistic *vs.* continuum descriptions of spherical NPs

The fluorescence response of PDI as adsorbed in L or T orientation on a spherical NP (see Fig. 1a) is studied. In particular, the attention is focused on the first bright excitation (HOMO–LUMO), which is associated with a $\pi \rightarrow \pi^*$ transition with the transition dipole moment aligned with the principal axis of the chromophore (see Fig. 1b).

In Fig. 2, calculated QM/ωFQFμ and QM/BEM Γ^r and Γ^{nr} are reported (in logarithmic scale) as a function of the PDI-Au NP distance and Au NP radius for both L and T orientations (panels a and b, respectively). The results for Ag NPs are similar and are reported in Fig. S1 and S2 of the ESI.†

Let us first focus on Γ^r. For the L orientation (see Fig. 2a, both QM/ωFQFμ and QM/BEM Γ^r decrease as the PDI-NP distance increases, converging at large distances to the gas-phase Γ^r value. This is because, in such a configuration, the PDI transition dipole moment and the plasmon dipole moment are parallel. As a result, the plasmon-induced Γ^r is larger than its gas-phase counterpart and decreases as a function of the PDI-NP distance because the interaction between the two parts vanishes at large separations ($\tilde{d}^{KO}_{plas} \rightarrow 0$). For the same reasons, by enlarging the NP size, Γ^r increases because the associated $\tilde{d}^{KO}_{plas}$ increases. It is worth remarking that QM/ωFQFμ and QM/BEM results are in almost perfect agreement, also from the quantitative point of view.

In contrast, for the T configuration (Fig. 2b), different trends are observed depending on the NP size. In fact, for small NPs (radius ≤ 10 Å), QM/ωFQFμ and QM/BEM Γ^r increase as the PDI-NP distance increases. For larger NPs (radius > 10 Å), QM/ωFQFμ and QM/BEM Γ^r decrease at small distances (<25 Å) and then increase at larger distances, displaying a minimum. In particular, by increasing the NP radius, the minimum shifts towards larger distances. In all cases, at large distances, the gas-phase Γ^r is recovered. These findings can be explained by considering that in T configuration the NP plasmon dipole moment and PDI transition dipole moment are anti-parallel. As a consequence, when $|\mathbf{d}^{KO}_{plas}| > |\mathbf{d}^{KO}_{mol}|$ Γ^r decreases (small distances), while when $|\mathbf{d}^{KO}_{plas}| < |\mathbf{d}^{KO}_{mol}|$ Γ^r increases (large distances). Γ^r minimum is displayed when $|\mathbf{d}^{KO}_{plas}| \simeq |\mathbf{d}^{KO}_{mol}|$. By increasing the NP radius, a larger induced NP dipole is obtained, shifting the Γ^r minimum to larger distances. In this

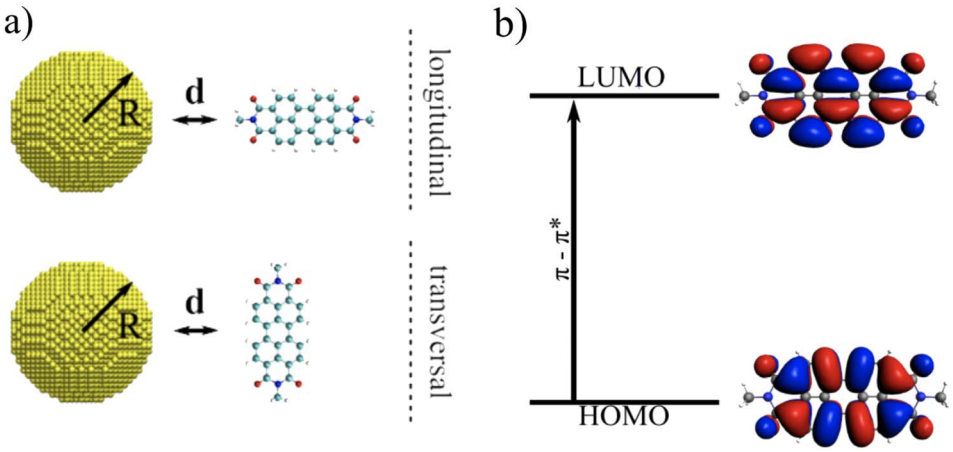

Fig. 1 (a) Graphical depiction of PDI interacting with a spherical NP of radius **R**. PDI is placed at a distance **d** from the NP in longitudinal (top) and transversal (bottom) configurations. (b) PDI molecular orbitals involved in the electronic transition under study.

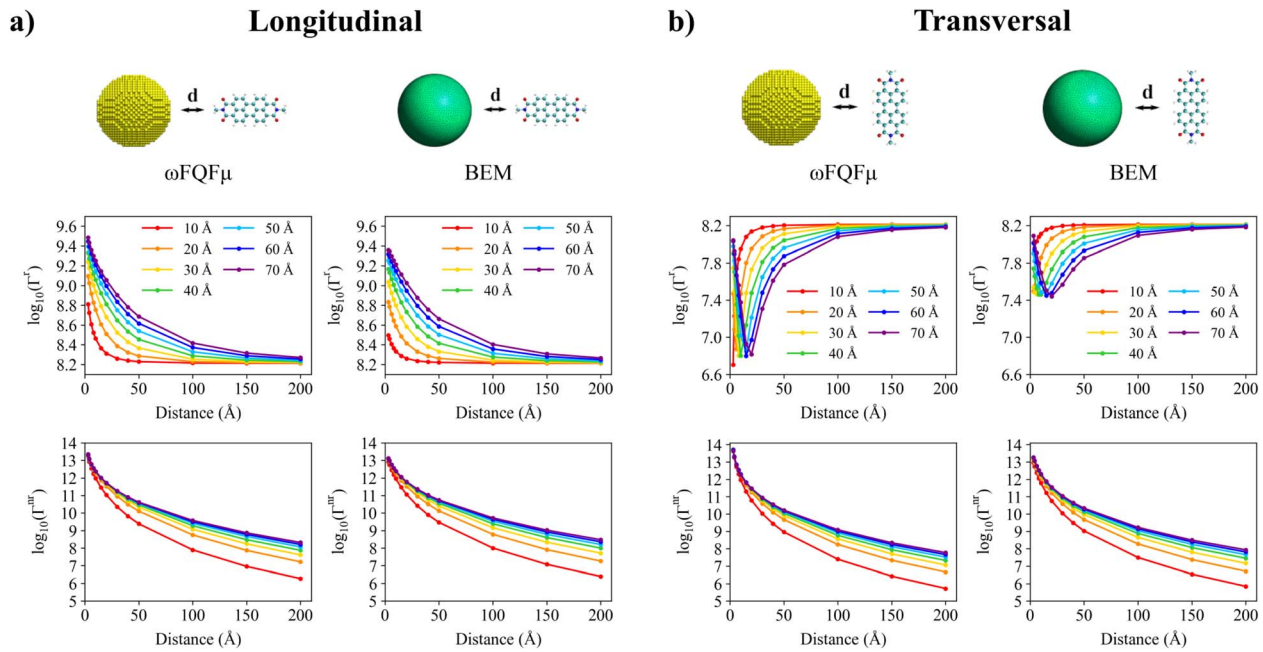

Fig. 2 Longitudinal (a) and transversal (b) orientations of PDI interacting with a spherical Au NP studied at the QM/ωFQFμ (left) and QM/BEM (right) levels (see top panel). Radiative (middle) and nonradiative (bottom) decay rates (logarithmic scale) as a function of the PDI-NP distance as obtained by varying the NP radius (from 10 Å to 70 Å).

case, QM/ωFQFμ and QM/BEM agreement is only qualitative. This can be related to the different plasmonic properties provided by the two approaches, *i.e.* different PRFs and different absorption profiles (see Fig. S3 of the ESI†). To investigate how the atomistic features of the NP surface affect the computed QM/ωFQFμ Γ^{r}, in Fig. S4 of the ESI† we report a scan over the NP-PDI angle (from 0 to 180°, with a step of 20°) for T disposition. Specifically, for NPs with a radius of 20 Å and 70 Å, PDI is positioned at the distance corresponding to the minimum of Γ^{r} (6 and 20 Å, respectively). Our findings reveal small and periodic fluctuations of Γ^{r} as a function of the angle, which are reduced as the NP size increases, highlighting the weaker impact of atomistic details as the structure approximates that of a perfect sphere. Thus, the numerical discrepancies between QM/ωFQFμ and QM/BEM reported in Fig. 2b mostly arise from the diverse modeling of the optical response of the NPs, rather than the atomistic features of the NP surface.

Remarkably, computed results are in agreement with experimental findings,[18,68–70] and are consistent with similar analysis performed at the semi-empirical ZINDO/BEM level,[27] thus demonstrating the reliability of ωFQFμ.

QM/ωFQFμ and QM/BEM Γ^{nr} display a similar behavior for both L and T configurations (see Fig. 2a and b). In particular, Γ^{nr} decreases as the PDI-NP distance increases for all considered NPs and approaches zero. Indeed, PDI non-radiative decay channels are neglected; thus, Γ^{nr} vanishes in the gas phase limit. At small distances, Γ^{nr} assumes almost the same value for all NP radii because the NP can be approximated as an infinite plane surface. At larger distances, Γ^{nr} increases for large NP sizes because a large dipole moment is induced on the NP (see eqn (6)). Remarkably, at large distances, and for all NP size, Γ^{nr} follows a distance^{-6} trend, following the Förster limit. These findings are again in agreement with previous computational investigations.[27]

To conclude this section, the relative brightness Φ^{RB} is evaluated. In Fig. 3, Φ^{RB} of PDI adsorbed in L configuration on Au (a) and Ag (b) spherical NPs are reported, as calculated at the QM/ωFQFμ (left) and QM/BEM (right) levels. In particular, Φ^{RB} dependence on the NP radius and PDI-NP distance is studied and graphically depicted as a 3D plot. It can be noticed that, for Au NPs, Φ^{RB} decreases by increasing the radius for a specific PDI-NP distance. For a fixed radius, Φ^{RB} shows the opposite trend, *i.e.*, it increases by increasing the PDI-NP separation. Thus, for Au NPs, a general quenching effect is obtained at both QM/ωFQFμ and QM/BEM levels. For Ag NPs, an increment in Φ^{RB} is observed by enlarging the PDI-NP distance, similarly to Au NPs. In contrast, Φ^{RB} behavior as a function of the NP radius is more complex and displays a minimum, which is shifted at larger radii as the PDI-NP distance increases. The different Ag–Au trends can be ascribed to the diverse plasmonic properties of the two materials. In fact, the absorption/emission PDI frequencies are close to Au PRF and fall in the pre-resonant region for Ag NPs. Consequently, the non-radiative decay channels are facilitated by Au NPs, thus yielding larger Γ^{nr} than Γ^{r} and A (see eqn (14)), finally resulting in Φ^{RB} reduction.[27,28] A similar investigation for the T orientation is reported in Fig. S5 of the ESI,† for which a less pronounced quenching effect is observed, in agreement with experimental findings.[18,68–70]

4.2 QM/ωFQFμ for complex-shaped nanostructures

4.2.1 Effect of the NP morphology. In this section, QM/ωFQFμ is applied to the study of the fluorescence response of PDI induced by complex-shaped Au NPs. Ih and cTO

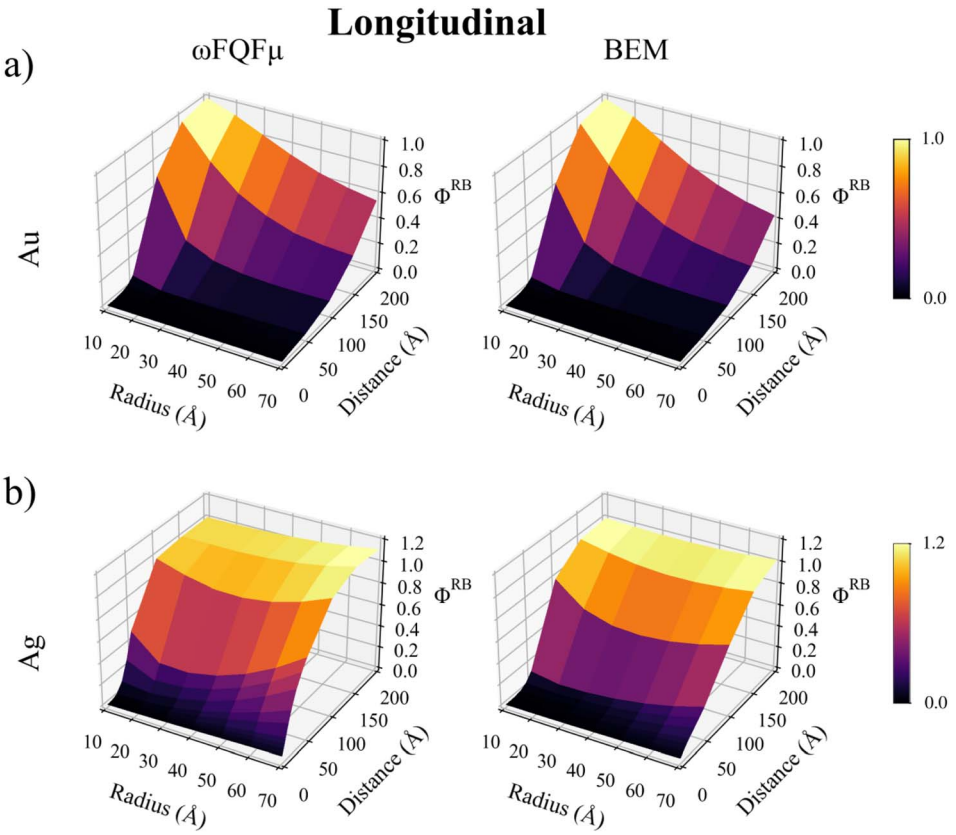

Fig. 3 QM/ωFQFμ (left) and QM/BEM (right) Φ^{RB} as a function of PDI-NP distance and NP radius for PDI in L orientation interacting with a spherical Au (a) and Ag (b) NP.

morphologies are considered; they feature sharp edges and atomistically defined tips, which require fully atomistic descriptions to be appropriately modeled. In fact, continuum BEM descriptions can lead to large numerical instabilities for these morphologies.[29,71]

In Fig. 4(i and j), QM/ωFQFμ Γ^{r}, Γ^{nr}, and Φ^{RB} values are reported as a function of the PDI-NP distance. *A* values are not given, because their trend is similar to Γ^{r}. PDI lays in the L orientation in the vicinity of spherical, Ih and cTO NPs with a radius of 30 Å. To highlight how different morphologies affect the fluorescence parameters, the differences between Γ^{r}, Γ^{nr}, and Φ^{RB} values for the various morphologies and the data for the spherical case are computed as follows:

$$\%X = \left(\frac{X_{\mathrm{Ih/cTO}}}{X_{\mathrm{sph}}} - 1\right) \times 100, \quad X = \left\{\Gamma^{r}, \Gamma^{nr}, \Phi^{RB}\right\} \qquad (15)$$

where $X_{\mathrm{Ih/cTO}}$ and X_{sph} indicate Γ^{r}, Γ^{nr}, Φ^{RB} values computed for Ih or cTO, and spherical NPs, respectively.

$\%\Gamma^{nr}$ maximum value occurs when PDI is close to Ih/cTO NPs and rapidly decreases until it reaches a plateau. In fact, for large distances, both $\Gamma^{nr}_{\mathrm{Ih/cTO}}$ and $\Gamma^{nr}_{\mathrm{sph}}$ values follow a Förster-like behavior ($\propto$distance^{-6}), and thus $\%\Gamma^{nr}$ converges to a finite value (see eqn (15)). $\%\Gamma^{r}_{\mathrm{Ih/cTO}}$ instead presents lower values than the spherical reference, smoothly converging towards zero as the PDI-NP distance increases. The combination of Γ^{r} and Γ^{nr} variation profiles as a function of the distance determines the $\%\Phi^{RB}$ function, which exhibits a maximum in the distance region between 50 and 100 Å. Indeed, $\%\Phi^{RB}$ profile is related to the intersection point of $\%\Gamma^{r}$ and $\%\Gamma^{nr}$ curves. Furthermore, Fig. 4(i and j) shows a substantial $\%\Phi^{RB}$ reduction at short distances (<30 Å) for both Ih and cTO morphologies. In this region, $\%\Gamma^{r}$ displays its lowest values while $\%\Gamma^{nr}$ reaches its maximum, overall favoring the quenching of the fluorescence signal. This behavior is due to the significant enhancement of the electric field near the sharp tips of cTO and Ih NPs.[33,35] Although these results show the same general behavior for Ih and cTO NPs, some subtle differences are worth discussing. Specifically, $\%\Gamma^{nr}$ is smaller for cTO than for Ih, and consequently, cTO $\%\Phi^{RB}$ is slightly larger.

To deepen the analysis, how a variation in the NP size affects the fluorescence response is investigated. To this end, Ih, cTO and spherical NPs with radii ranging from 10 to 70 Å are studied (see Fig. 4(c–h), and S6 and S7 in the ESI†). First, the NP size highly affects both $\%\Gamma^{nr}$ and $\%\Gamma^{r}$. In fact, for short PDI-NP distances, $\%\Gamma^{nr}$ increases, while the opposite holds for $\%\Gamma^{r}$. This results in a substantial decrease in $\%\Phi^{RB}$ in this distance region. At larger distances (50–100 Å), both morphologies display fluorescence responses that largely exceed that obtained for the reference spherical NPs, reaching a maximum that shifts toward larger distances and decreases in intensity by increasing NP size. Fig. 4(g and h) clearly shows that the discrepancies between the cTO and Ih become more pronounced for small NP radii. In fact, within this size range, the atomistic differences in Ih/cTO morphologies are more significant. The radius dependence of the $\%\Phi^{RB}$ maxima originates from a slight mismatch

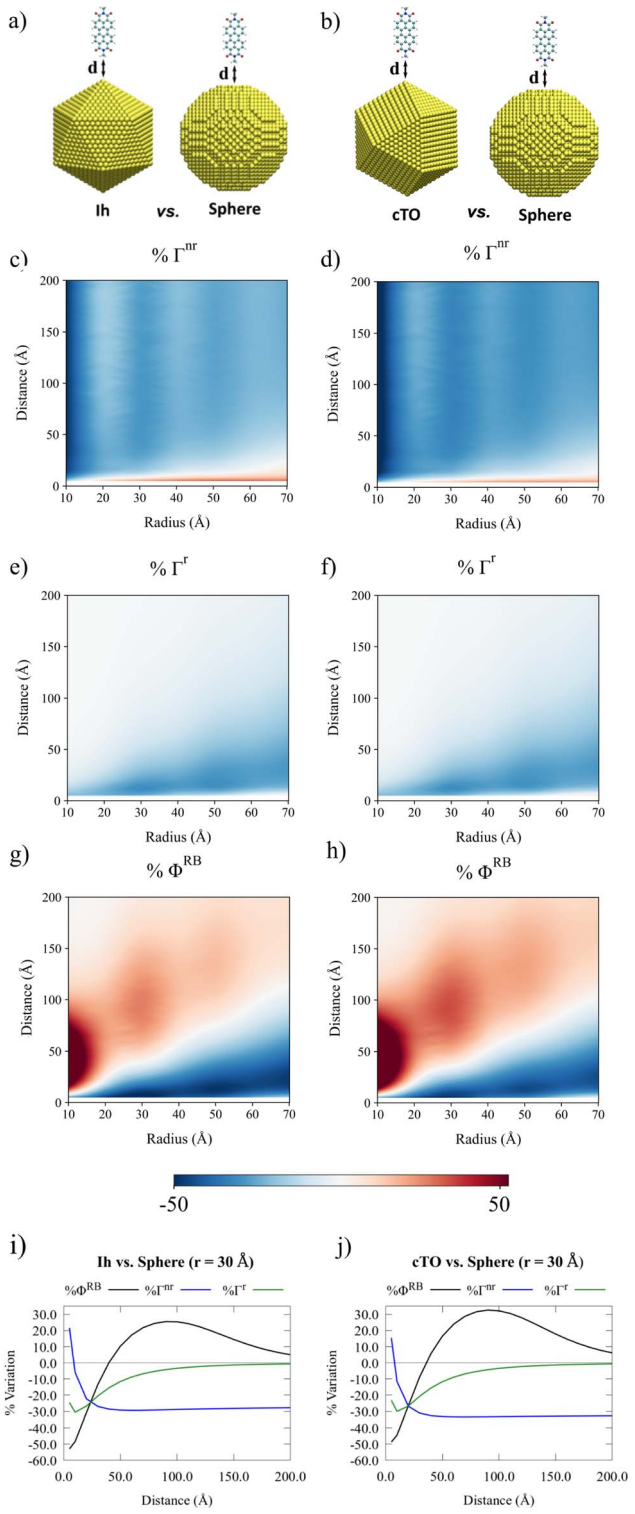

Fig. 4 Graphical representation of PDI interacting with Au Ih (a) and cTO (b) NPs, compared with spherical NPs. QM/ωFQFμ $\%\Gamma^{nr}$ (c and d), $\%\Gamma^{r}$ (e and f), and $\%\Phi^{RB}$ (g and h) 2D color plots as a function of the PDI-NP distance and NP radius for Ih *vs.* sphere and cTO *vs.* sphere systems, respectively. QM/ωFQFμ $\%\Gamma^{nr}$, $\%\Gamma^{r}$, and $\%\Phi^{RB}$ values for systems of 30 Å radius are displayed in panels (i) (Ih *vs.* sphere) and (j) (cTO *vs.* sphere).

in the effective sphere-cTO/Ih size due to the atomistically defined structures (see Tables S1 and S2 of the ESI †for the effective size of the studied structures). To avoid the maxima fluctuations reported in Fig. 4(g and h), we have performed the same study by relying on a linear interpolation of the Φ^{RB} values on the effective radius of the spherical NPs corresponding to the effective radius of cTO NPs (see Fig. S8 in the ESI†).

4.2.2 Dependence of fluorescence response on the chromophore-NP configuration. To further demonstrate the versatility of QM/ωFQFμ, how the relative configuration of the molecule-NP system affects the fluorescence response is here evaluated. The possibility of performing this kind of investigation is a remarkable feature of the fully atomistic nature of the method.

In Fig. 5, Φ^{RB} and $\%\Phi^{RB}$ as a function of PDI-NP distance and the PDI-NP configuration are graphically depicted. In particular, the PDI moiety is adsorbed in L orientation on the tip (T), side (S), and face (F) of both Ih (a) and cTO (b) NPs of 30 Å radius. As a comparison, the PDI adsorbed on a spherical NP of equal size (30 Å radius) is also reported. QM/ωFQFμ results show that, for both Ih and cTO, the highest deviation in the fluorescence response compared to the spherical reference is obtained for the T configuration. This is not unexpected, and it is due to the largely inhomogeneous electric field near the sharp interfaces of the metal structures.[34] The fully atomistic nature of the model can also capture the smaller differences, that are instead reported for S and F configurations. In particular, such differences become more pronounced when moving from Ih to cTO NPs (see $\%\Phi^{RB}$ in Fig. 5, bottom). This is due to the alternating triangular and squared faces in the cTO structure, which accentuates the inhomogeneity of the near-field.

4.2.3 PDI interacting with Ag nanorods. The previous sections have focused on the capacity of Au NPs to quench the fluorescence signal emitted by a nearby chromophore. Several strategies can be exploited to enhance the fluorescence response, *i.e.* the relative brightness Φ^{RB}. For instance, fluorescence enhancement can be obtained by increasing the size of the nanostructures, which makes Γ^{r} to be dominant over Γ^{nr} (see eqn (14)) due to the increased NP dipole moment.[27,72] Another possibility is to consider NPs exhibiting a PRF close (in energy) to an electronic absorption of the chromophore.[27–29] This results in a more efficient absorption process, leading to a higher population of the excited states and, consequently, a higher emission probability.

To investigate this aspect, the fluorescence response of PDI in the proximity of silver nanorods (SNRs) is studied. Indeed nanorods have been amply exploited experimentally to enhance fluorescence signals. In fact, their PRF can be easily tuned by varying their aspect ratio.[73–76] Notably, ωFQFμ can accurately reproduce nanorod's PRF values.[33]

In Fig. 6(b), absorption cross-section are reported for two SNRs with fixed radius ($\mathbf{r} = 18.5$ Å) and two lengths ($\mathbf{L} = 149.5$ Å and $\mathbf{L} = 154$ Å; see Fig. 6(a)). The absorption spectrum is dominated by a main plasmonic peak, associated with the dipolar plasmon. As expected, by increasing the SNR length, the PRF redshifts of about 0.04 eV. The plasmonic response sensitivity as a function of the SNR length can be exploited to match absorption (ω_{abs}) or emission (ω_{em}) PDI frequencies.

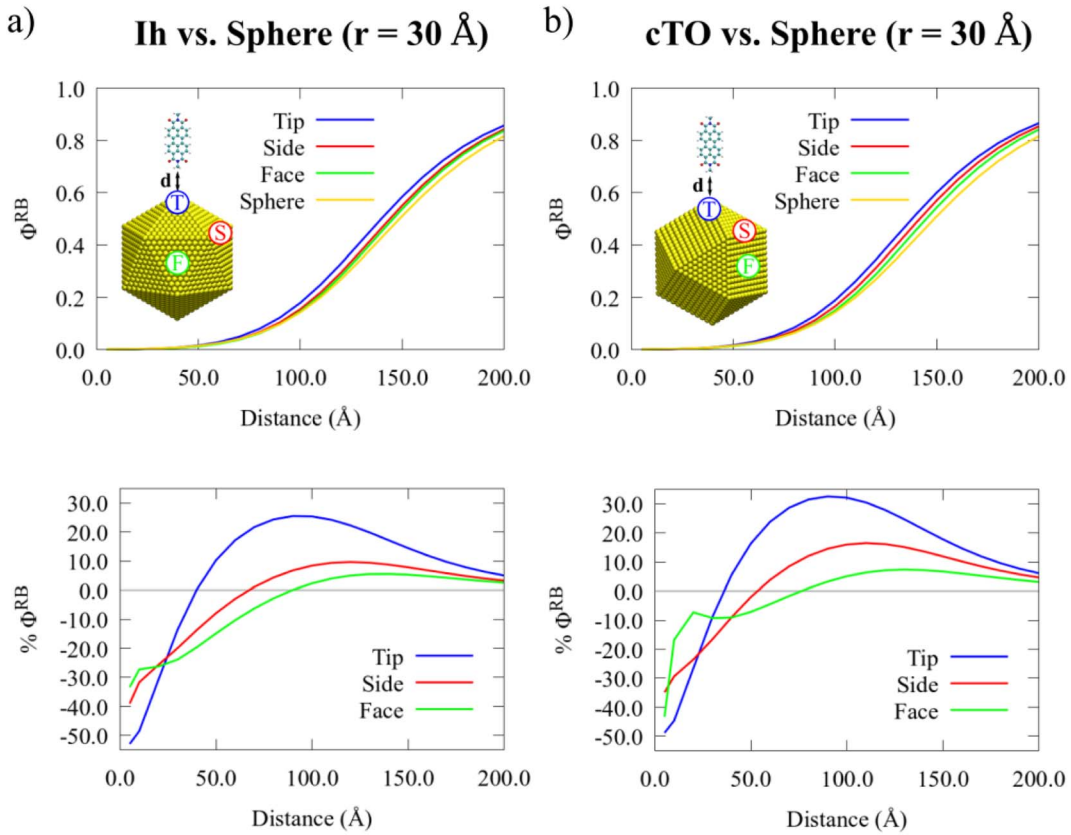

Fig. 5 QM/ωFQFμ Φ^{RB} (top) and $\%\Phi^{RB}$ (bottom) as a function of the PDI-NP distance for tip, side, and face PDI adsorption geometries. Ih (a) and cTO (b) NP morphologies are studied and compared to spherical NPs.

PDI Φ^{RB} values as a function of the SNR-PDI distance are also given in Fig. 6(c)) for both nanorods. As expected, the highest fluorescence enhancement is reported when the PRF coincides with ω_{abs}. However, a large fluorescence enhancement is also obtained when PRF aligns with ω_{em}. Although Φ^{FQY} values computed in the two cases are almost identical (see eqn (14)), the energy similarity of ω_{abs} and ω_{em} and the large SNR dipole moment lead to enhanced A values.

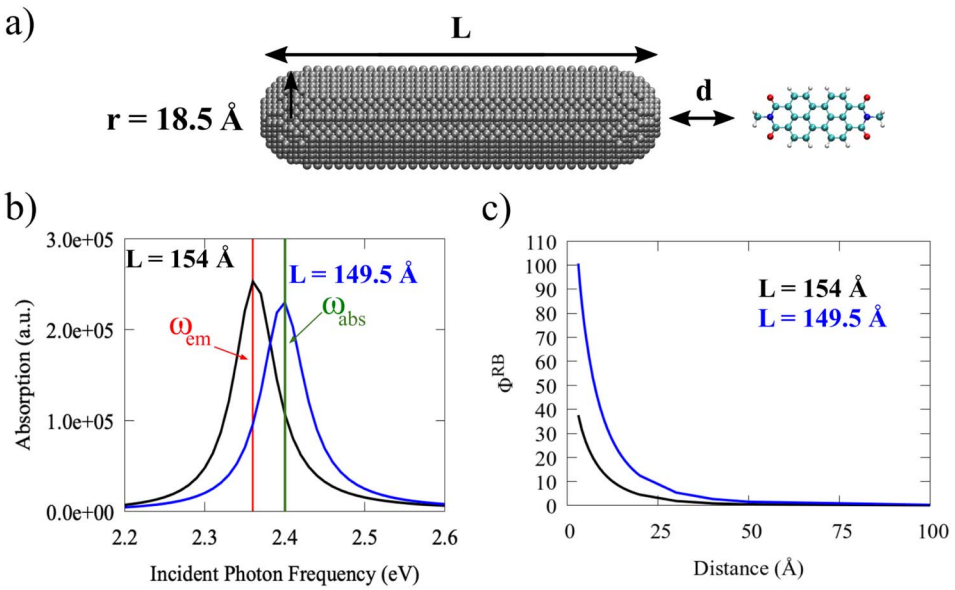

Fig. 6 (a) Geometrical representation of the studied SNRs interacting with PDI. (b) PRF of a SNRs with 18.5 Å radius (r) as function of the length (L). PDI emission (ω_{em}) and absorption (ω_{abs}) frequencies are marked with vertical red and green lines, respectively. (c) PDI Φ^{RB} as a function of PDI-SNR distance for L = 149.5 Å and L = 154 Å.

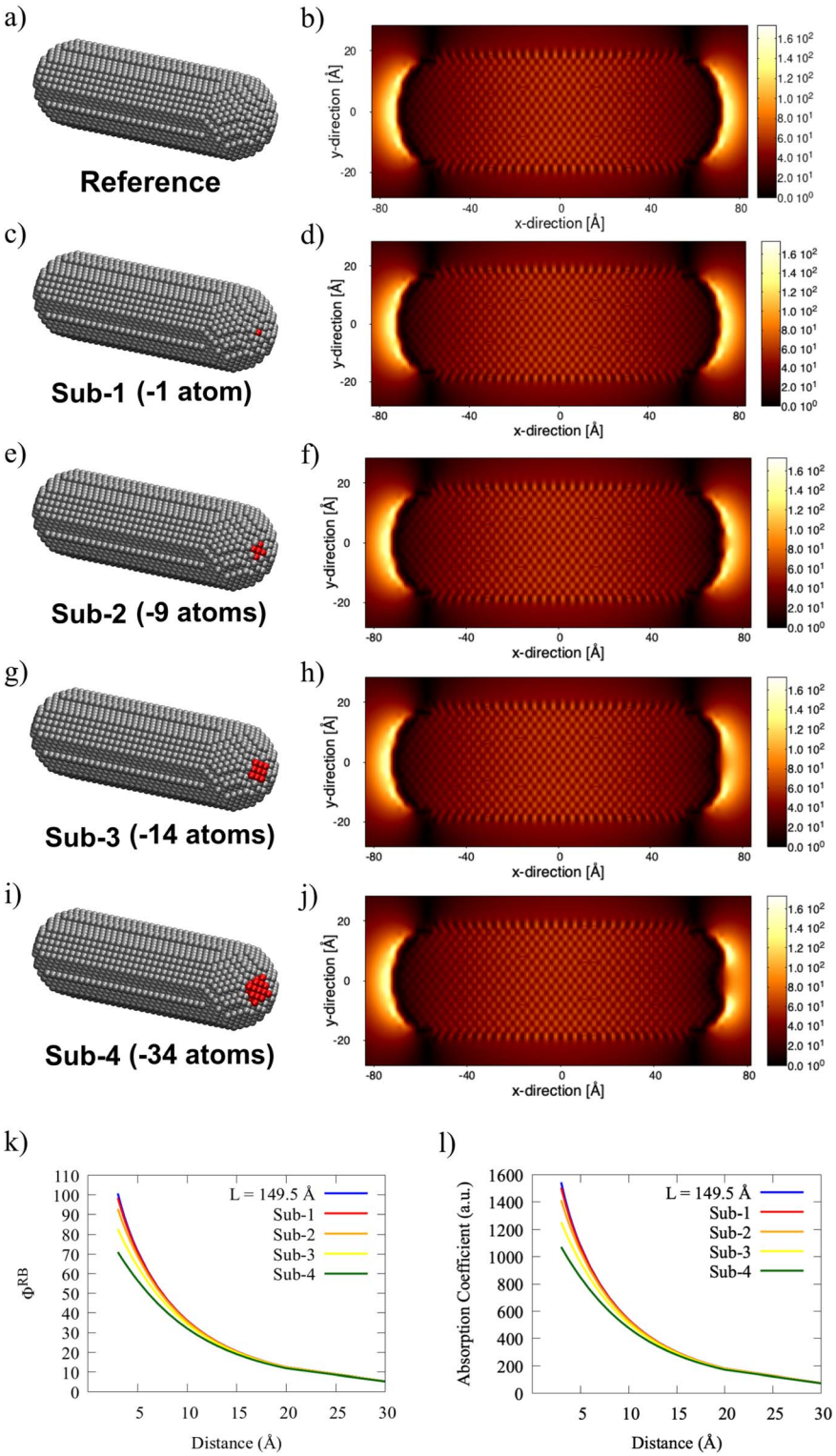

Fig. 7 (a) Graphical depiction of SNR pristine (a), r = 18.5 Å; L = 149.5 Å) and defected structures (c, e, g and i), as obtained by atomistic deletions at the SNR end (see red regions). The number of removed atoms is also reported for each structure. The associated ωFQFμ electric field enhancement 2D color maps, obtained at the PRF for a field polarization along the principal axis, are given in panels (b, d, f, h and j). (k) QM/ωFQFμ Φ^{RB} and *A* (l) values as a function of the PDI-SNR distance.

Let's focus on how SNR atomistic structure close to PDI affects the molecular Φ^{RB}. Fig. 7 provides a graphical representation of such structure modifications, which are obtained by digging the SNR end close to PDI with a concentric (with nanorod axis) sphere with increasing radius. This results in the removal of SNR atoms within the volumes spanned by the

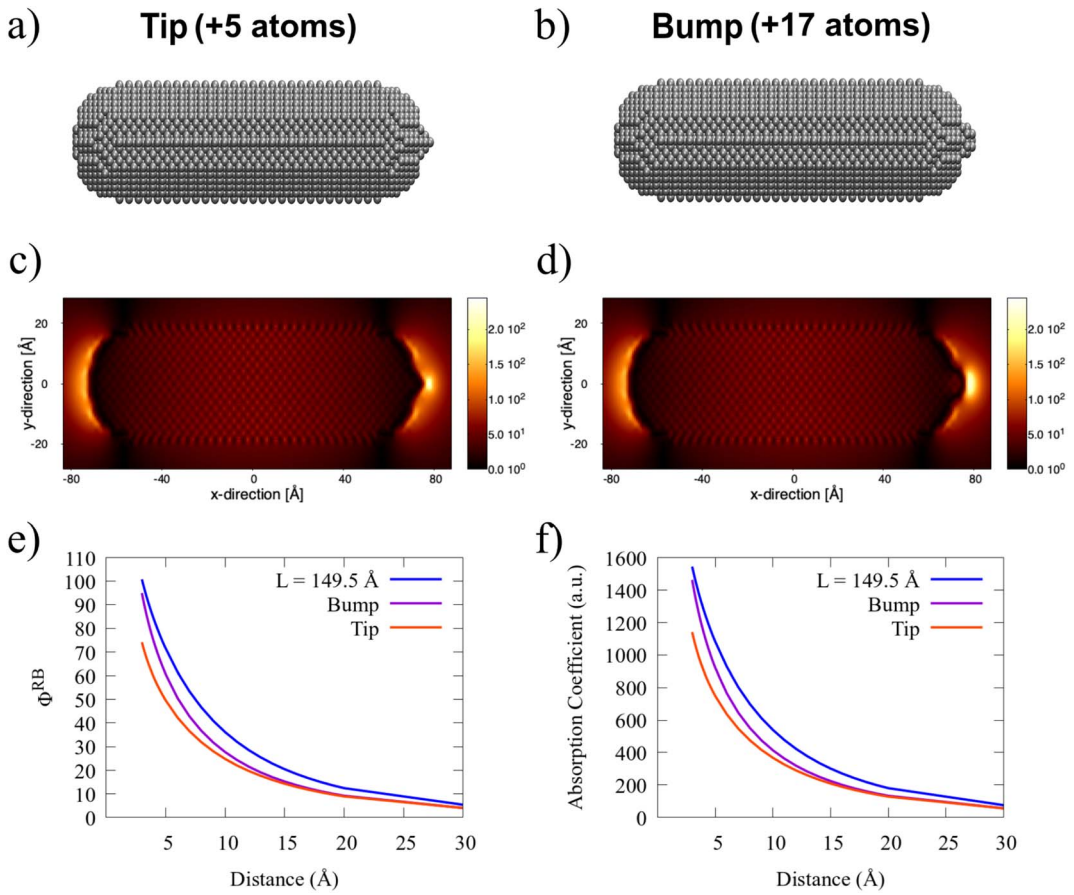

Fig. 8 (a) Graphical depiction of SNRs featuring an atomistic tip (a) and a bump (b). The number of added atoms compared to the pristine SNR (r = 18.5 Å; L = 149.5 Å) is also reported for each structure. The associated ωFQFμ electric field enhancement 2D color maps, obtained at the PRF for a field polarization along the principal axis, are given in panels (c and d). (e) QM/ωFQFμ Φ^{RB} and *A* (f) values as a function of the PDI-SNR distance.

selected spheres. In particular, the number of the removed atoms for the four studied geometrical modifications (Sub-1–Sub-4) are given in Fig. 7(c, e, g and i), where they are also highlighted in red. The electric field enhancement color maps associated with each SNR are also reported. Following ref. 33, the latter are calculated as the ratio between the magnitude of the induced and the incident electric fields. The external field is polarized along the SNR principal axis and oscillates at the dipolar PRF of each structure ($\omega = 2.40$ eV). Color maps clearly show that the maximum field enhancement is obtained at the two SNR ends. By digging the SNR right end, a substantial reduction of the electric field enhancement in the deletion region is reported.

Fig. 7(k) shows the impact of these atomistic modifications on Φ^{RB} as a function of the PDI-SNR distance as compared to the reference SNR (**L** = 149.5 Å). Clearly, the largest discrepancies emerge at small PDI-SNR distances. In particular, the structures characterized by the highest atomistic deletions (Sub-3 and Sub-4) feature a substantial reduction in Φ^{RB} values. This is expected and is related to the modifications in the local field enhancement (see Fig. 7(h and j)). Indeed, Γ^{r} and Γ^{nr} variations as a function of PDI-SNR distance have small effect on Φ^{FQY}. Thus, the reported differences primarily originate from the changes in *A* as a function of the PDI-NP distance (see eqn (14) and Fig. 7(l)).

An opposite structural modification is also possible, *i.e.*, the increasing of the SNR end close to the PDI with a small sharp tip – +5 atoms – or a spherical bump – +17 atoms (see Fig. 8(a and b)). Both systems feature a larger and more localized enhanced field than the pristine SNR (see Fig. 8(c and d) and 7(b)). In particular, the most localized enhanced field is obtained for the tip-SNR due to its sharp profile. Fig. 8(e) shows Φ^{RB} values of PDI placed at the proximity of both systems as a function of the PDI-SNR distance, taking the full SNR (**L** = 149.5 Å) as a reference. Tip-SNR and bump-SNR are both associated with a significant Φ^{RB} reduction, especially for small PDI-SNR distances. In particular, the largest discrepancy with the reference is given by Tip-SNR, for which the computed fluorescence response is comparable with the Sub-4 system (see Fig. 7(k)). For both geometrical modifications, the overall quenching of the fluorescence signal is due to the smaller SNR dipole compared to the reference, which results in a lower absorption coefficient *A* (see eqn (14) and Fig. 8(f)). It is worth mentioning that the structural modifications of the SNR only modify their electrical properties but not their absorption profile compared to the pristine structure (see Fig. S9 in the ESI†).

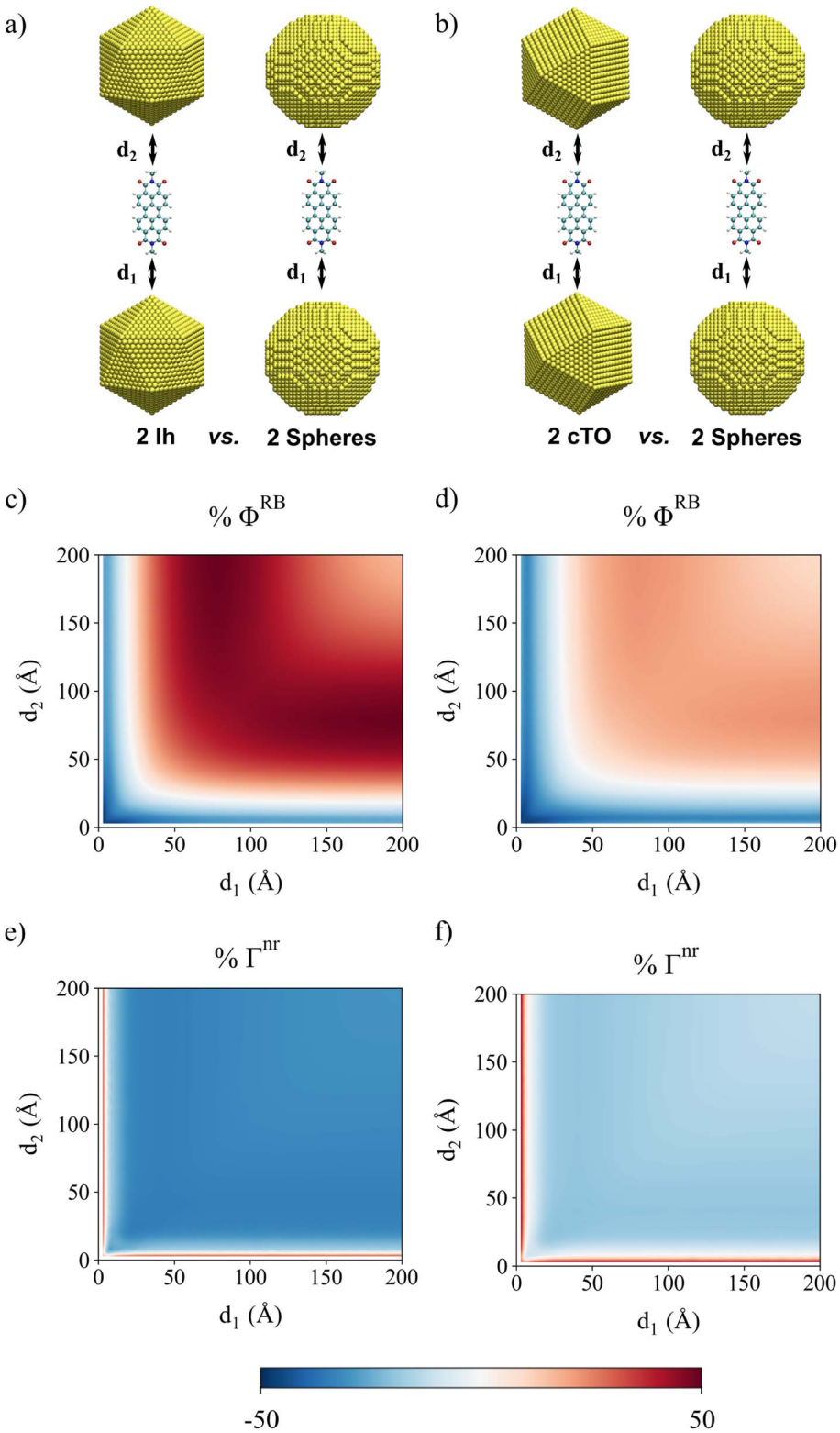

Fig. 9 Graphical representation of PDI interacting with Au Ih (a) and cTO (b) dimers, as compared with spherical NP dimers (radius 30 Å). QM/ωFQFμ $\%\Phi^{RB}$ (c and d), $\%\Gamma^{nr}$ (e and f) 2D color plots as a function of the distances between PDI and the two NPs, for Ih *vs.* sphere and cTO *vs.* sphere systems, respectively.

To underscore the importance of a fully atomistic modeling of the substrate, in Fig. S10 in the ESI† we replicate the simulations reported in Fig. 7 and 8 by exploiting the continuum QM/BEM approach. Specifically, we study the longitudinal absorption, Φ^{RB}, and Φ^{FQY} of pristine SNR ($\mathbf{r} = 18.5$ Å; $\mathbf{L} = 149.5$ Å), as well as those featuring a tip, bump, and the Sub-4 cavity.

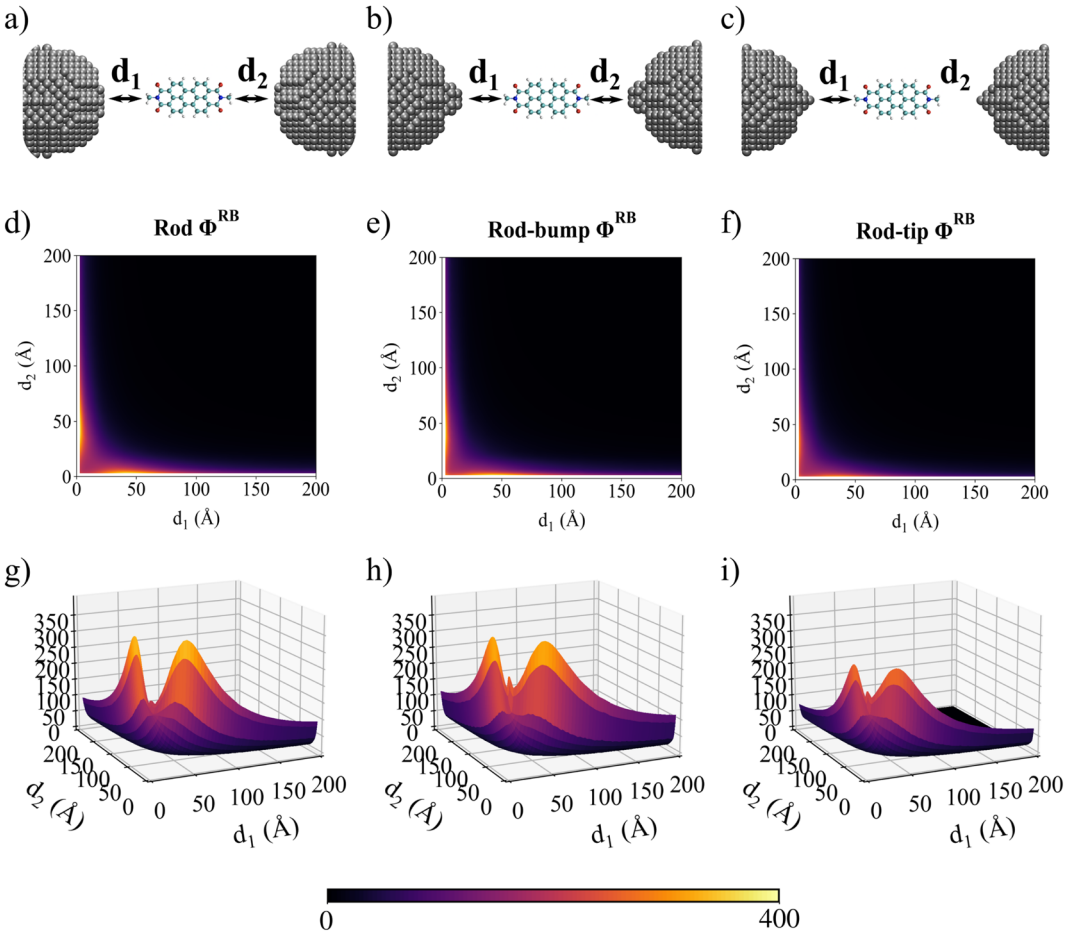

Fig. 10 Graphical depiction of PDI interacting with two pristine Ag SNRs (a), two Ag SNRs featuring bumps (b) and tips (c). QM/ωFQFμ Φ^{RB} (d–f) and Φ^{RB} (g–i) 2D and 3D color maps as a function of the distances between PDI and the two SNRs.

Additionally, we evaluate three different discretizations of the surfaces (~10 000,~5000, ~1000 tesserae) for each system. Our findings reveal a strong dependence on the number of tesserae used to describe the BEM surface. In particular, while the longitudinal PRFs tend to converge after 5000 tesserae, computed Φ^{RB} and Φ^{FQY} with 5000 and 10 000 tesserae show a mismatch as a function of the SNR-PDI distance. Focusing on the structure presenting the Sub-4 cavity, results suggest strong numerical instabilities when increasing the number of tesserae. This is evidenced by the lower-energy band emerging in the longitudinal absorption plots, along with the Φ^{FQY} trend which presents an anomalous peak instead of the expected gradual decrease with increasing the SNR-PDI separation.

4.2.4 PDI interacting with NP dimers. This section finally focuses on the fluorescence response of PDI interacting with two NPs. As a first case study, PDI in L configuration is sandwiched between two spherical, Ih, or cTO Au NPs with a radius equal to 30 Å (see Fig. 9(a and b)). The fluorescence response is investigated in terms of the Φ^{RB} percentage variation (see eqn (15)) of Ih/cTO NPs compared to spherical NP, as a function of PDI distance from each NP (d_1 and d_2). The results are graphically depicted in Fig. 9(c and d) (see Fig. S11 in the ESI† for the same representation in 3D) for both cTO and Ih NPs. First, % Φ^{RB} values computed for Ih or cTO NPs follow the same trend. In fact, for small d_1 and d_2, $\%\Phi^{RB}$ reaches a minimum while at larger distances (≥50 Å), both morphologies display fluorescence responses that largely exceed that obtained for the reference spherical NP. In fact, $\%\Phi^{RB}$ reaches a maximum (~40 for Ih and ~ 20 for cTO) that decreases in intensity by increasing d_1 and d_2. Notably, larger $\%\Phi^{RB}$ values are observed for Ih than cTO. These findings are opposite from what is reported for a single NP (see Fig. 4(i and j)). This is due to the lower Γ^{nr} reported for Ih dimer (Fig. 9(e and f)), which reduces the quenching efficiency (absolute values of Φ^{RB} are always lower than 1).

A similar study can be performed by considering PDI interacting with SNR dimers, composed of two reference cylindrical pristine SNRs (**r** = 18.5 Å; **L** = 149.5 Å), two tip-SNRs, and two bump-SNRs (see Fig. 10(a–c)). PDI Φ^{RB} as a function of the distances compared to the two SNRs is studied (see Fig. 10(d–i)). For all shapes, the maximum Φ^{RB} values are obtained when d_1 and d_2 differ (anti-symmetrical displacement). Significant discrepancies compared to the pristine SNR emerge when the bump and the tip are introduced. Specifically, for the bump-SNR, the maximum Φ^{RB} values are similar to the pristine SNR, while a large Φ^{RB} increase is obtained at $d_1 = d_2 = 3$ Å. This

is also observed for the tip-SNR dimer. However, consistently smaller Φ^{RB} values compared to the reference structure are reported in this case. Remarkably, these findings are in agreement with the results already discussed for single SNR NPs.

To conclude this section, it is worth highlighting that the Φ^{RB} observed profiles for Au and Ag dimers are related to the different physicochemical mechanisms governing the fluorescence process. In the Au dimer setup, the fluorescence response is primarily driven by the relative variation of decay rates Φ^{FQY}, whose trend perfectly matches Φ^{RB} behavior (see Fig. S12 in the ESI†). In fact, the maximum fluorescence signal is obtained when a symmetrical arrangement ($d_1 = d_2$) is considered. A fluorescence enhancement can potentially be achieved at small distances by increasing the size of the NP, until reaching the critical point where Γ^{r} dominates over Γ^{nr}.[27] On the contrary, the influence of SNRs on Φ^{RB} is primarily determined by the variations of A as a function d_1 and d_2 (see Fig. S13 of the ESI†), which provide a one-to-one correspondence with Φ^{RB} trends reported in Fig. 10(d–i). Thus, in this case, SNR antisymmetrical arrangements ($d_1 \neq d_2$) are crucial in enhancing the fluorescence signal.

5 Conclusions

In the present work, the QM/ωFQFμ formalism has been extended for the first time to study the fluorescence signal of molecular systems close to plasmonic substrates. The approach fully retains the atomistic structure of both the chromophore and the nanostructure, thus allowing the description of how NP atomistic features affect the molecular response.

To demonstrate the reliability of the novel methodology, the fluorescence response of a well-studied fluorophore, PDI, in the presence of plasmonic Ag and Au NPs, is investigated. In particular, diverse NP morphologies are considered, ranging from spherical NPs to complex-shaped NPs, such as Ih and cTO NPs, atomistically defected nanorods and NP dimers. The reported findings show that sharp edges, associated with highly localized induced electric fields, play a crucial role in determining the molecular fluorescence response. Remarkably, this can be accurately described by only exploiting a fully atomistic approach as the one proposed in the present work. As a result, QM/ωFQFμ is here presented as an effective methodology to rationalize the fluorescence signals in atomistic-defined setups, such as for TEPL or picocavity-controlled SEF,[22,77,78] pending the development of a reliable computational protocol for the simulation of realistic nanostructures.

Finally, it is worth highlighting how significant fluorescence signal enhancement can be obtained by matching the PRF with the molecular absorption energy achieved by structural deformations on the NP. The findings of the present study underscore the fundamental role of a fully atomistic description for an in-depth understanding of the fluorescence response in the vicinity of complex-shaped nanostructures. Indeed, this work paves the way for the rational design and optimization of plasmonic devices to enhance the fluorescence response of target chromophores.

Conflicts of interest

There are no conflicts to declare.

Acknowledgements

The authors acknowledge Prof. Stefano Corni (Università di Padova) for useful discussion. The authors gratefully acknowledge the Center for High-Performance Computing (CHPC) at SNS for providing the computational infrastructure. CC acknowledges funding from MUR-FARE Ricerca in Italia: Framework per l'attrazione ed il rafforzamento delle eccellenze per la Ricerca in Italia - III edizione. Prot. R20YTA2BKZ, and from PNRR MUR project PE0000023-NQSTI.

References

1 M. Li, S. K. Cushing and N. Wu, Plasmon-enhanced optical sensors: a review, *Analyst*, 2015, **140**, 386–406.
2 M. Sharifi, F. Attar, A. A. Saboury, K. Akhtari, N. Hooshmand, A. Hasan, M. A. El-Sayed and M. Falahati, Plasmonic gold nanoparticles: Optical manipulation, imaging, drug delivery and therapy, *J. Controlled Release*, 2019, **311–312**, 170–189.
3 M. T. Yaraki and Y. N. Tan, Metal nanoparticles-enhanced biosensors: synthesis, design and applications in fluorescence enhancement and surface-enhanced Raman scattering, *Chem.–Asian J.*, 2020, **15**, 3180–3208.
4 M. G. Albrecht and J. A. Creighton, Anomalously intense Raman spectra of pyridine at a silver electrode, *J. Am. Chem. Soc.*, 1977, **99**, 5215–5217.
5 D. L. Jeanmaire and R. P. Van Duyne, Surface Raman spectroelectrochemistry: Part I. Heterocyclic, aromatic, and aliphatic amines adsorbed on the anodized silver electrode, *J. Electroanal. Chem. Interfacial Electrochem.*, 1977, **84**, 1–20.
6 A. Campion and P. Kambhampati, Surface-enhanced Raman scattering, *Chem. Soc. Rev.*, 1998, **27**, 241–250.
7 K. A. Willets and R. P. Van Duyne, Localized surface plasmon resonance spectroscopy and sensing, *Annu. Rev. Phys. Chem.*, 2007, **58**, 267–297.
8 R. Alvarez-Puebla, L. M. Liz-Marzán and F. J. García de Abajo, Light concentration at the nanometer scale, *J. Phys. Chem. Lett.*, 2010, **1**, 2428–2434.
9 E. Le Ru and P. Etchegoin, *Principles of Surface-Enhanced Raman Spectroscopy: and Related Plasmonic Effects*, Elsevier, 2008.
10 S. A. Maier, *Plasmonics: Fundamentals and Applications*, Springer Science & Business Media, 2007.
11 J. Langer, D. Jimenez de Aberasturi, J. Aizpurua, R. A. Alvarez-Puebla, B. Auguié, J. J. Baumberg, G. C. Bazan, S. E. J. Bell, A. Boisen, A. G. Brolo, J. Choo, D. Cialla-May, V. Deckert, L. Fabris, K. Faulds, E. C. García de Abajo, R. Goodacre, D. Graham, A. J. Haes, C. L. Haynes, C. Huck, T. Itoh, M. Käll, J. Kneipp, N. A. Kotov, H. Kuang, Le Ru, H. K. Lee, J.-F. Li, X. Y. Ling, S. A. Maier, T. Mayerhöfer, M. Moskovits, K. Murakoshi,

J.-M. Nam, S. Nie, Y. Ozaki, I. Pastoriza-Santos, J. Perez-Juste, J. Popp, A. Pucci, S. Reich, B. Ren, G. C. Schatz, T. Shegai, S. Schlücker, L.-L. Tay, K. G. Thomas, Z.-Q. Tian, R. P. Van Duyne, T. Vo-Dinh, Y. Wang, K. A. Willets, C. Xu, H. Xu, Y. Xu, Y. S. Yamamoto, B. Zhao and L. M. Liz-Marzán, Present and future of surface-enhanced Raman scattering, *ACS Nano*, 2019, **14**, 28–117.

12 J. L. Payton, S. M. Morton, J. E. Moore and L. Jensen, A discrete interaction model/quantum mechanical method for simulating surface-enhanced Raman spectroscopy, *J. Chem. Phys.*, 2012, **136**, 214103.

13 J. L. Payton, S. M. Morton, J. E. Moore and L. Jensen, A hybrid atomistic electrodynamics–quantum mechanical approach for simulating surface-enhanced Raman scattering, *Acc. Chem. Res.*, 2014, **47**, 88–99.

14 Z. Hu, D. V. Chulhai and L. Jensen, Simulating surface-enhanced hyper-Raman scattering using atomistic electrodynamics-quantum mechanical models, *J. Chem. Theory Comput.*, 2016, **12**, 5968–5978.

15 D. V. Chulhai, X. Chen and L. Jensen, Simulating ensemble-averaged surface-enhanced Raman scattering, *J. Phys. Chem. C*, 2016, **120**, 20833–20842.

16 R. R. Chance, A. Prock and R. Silbey, *Advances in Chemical Physics*, John Wiley & Sons, Ltd, 1978, pp. 1–65.

17 S. Garoff, D. A. Weitz, M. S. Alvarez and J. I. Gersten, Electrodynamics at rough metal surfaces: Photochemistry and luminescence of adsorbates near metal-island films, *J. Chem. Phys.*, 1984, **81**, 5189–5200.

18 B. Fu, J. D. Flynn, B. P. Isaacoff, D. J. Rowland and J. S. Biteen, Super-Resolving the Distance-Dependent Plasmon-Enhanced Fluorescence of Single Dye and Fluorescent Protein Molecules, *J. Phys. Chem. C*, 2015, **119**, 19350–19358.

19 J. Zheng, X. Cheng, H. Zhang, X. Bai, R. Ai, L. Shao and J. Wang, Gold Nanorods: The Most Versatile Plasmonic Nanoparticles, *Chem. Rev.*, 2021, **121**, 13342–13453.

20 Y. Jung, J. Kim, N. H. Kim and H. G. Kim, Ag–ZnO Nanocomposites as a 3D Metal-Enhanced Fluorescence Substrate for the Fluorescence Detection of DNA, *ACS Appl. Nano Mater.*, 2023, **6**, 976–985.

21 K.-Q. Lin, J. Yi, J.-H. Zhong, S. Hu, B.-J. Liu, J.-Y. Liu, C. Zong, Z.-C. Lei, X. Wang, J. Aizpurua, R. Esteban and B. Ren, Plasmonic photoluminescence for recovering native chemical information from surface-enhanced Raman scattering, *Nat. Commun.*, 2017, **8**, 14891.

22 B. Yang, G. Chen, A. Ghafoor, Y. Zhang, Y. Zhang, Y. Zhang, Y. Luo, J. Yang, V. Sandoghdar, J. Aizpurua, Z. Dong and J. G. Hou, Sub-nanometre resolution in single-molecule photoluminescence imaging, *Nat. Photonics*, 2020, **14**, 693–699.

23 H. Lee, D. Y. Lee, M. G. Kang, Y. Koo, T. Kim and K.-D. Park, Tip-enhanced photoluminescence nano-spectroscopy and nano-imaging, *Nanophotonics*, 2020, **9**, 3089–3110.

24 W. Peeters, S. Toyouchi, Y. Fujita, M. Wolf, B. Fortuni, E. Fron, T. Inose, J. Hofkens, T. Endo, Y. Miyata and H. Uji-i, Remote Excitation of Tip-Enhanced Photoluminescence with a Parallel AgNW Coupler, *ACS Omega*, 2023, **8**, 38386–38393.

25 S. Khatua, P. M. R. Paulo, H. Yuan, A. Gupta, P. Zijlstra and M. Orrit, Resonant Plasmonic Enhancement of Single-Molecule Fluorescence by Individual Gold Nanorods, *ACS Nano*, 2014, **8**, 4440–4449.

26 A. Rose, T. B. Hoang, F. McGuire, J. J. Mock, C. Cirací, D. R. Smith and M. H. Mikkelsen, Control of Radiative Processes Using Tunable Plasmonic Nanopatch Antennas, *Nano Lett.*, 2014, **14**, 4797–4802.

27 S. Vukovic, S. Corni and B. Mennucci, Fluorescence enhancement of chromophores close to metal nanoparticles. Optimal setup revealed by the polarizable continuum model, *J. Phys. Chem. C*, 2009, **113**, 121–133.

28 A. Sanchez-Gonzalez, S. Corni and B. Mennucci, Surface-Enhanced Fluorescence within a Metal Nanoparticle Array: The Role of Solvent and Plasmon Couplings, *J. Phys. Chem. C*, 2011, **115**, 5450–5460.

29 M. Romanelli, G. Dall'Osto and S. Corni, Role of metal-nanostructure features on tip-enhanced photoluminescence of single molecules, *J. Chem. Phys.*, 2021, **155**, 214304.

30 S. D. Catingan and A. Moores, Recent Progress in Surface-Enhanced Fluorescence Using Gold Nanorods, *ACS Appl. Nano Mater.*, 2024, DOI: **10.1021/acsanm.3c04756**.

31 L. L. Jensen and L. Jensen, Electrostatic Interaction Model for the Calculation of the Polarizability of Large Noble Metal Nanoclusters, *J. Phys. Chem. C*, 2008, **112**, 15697–15703.

32 N. Asadi-Aghbolaghi, R. Rüger, Z. Jamshidi and L. Visscher, TD-DFT+TB: An Efficient and Fast Approach for Quantum Plasmonic Excitations, *J. Phys. Chem. C*, 2020, **124**, 7946–7955.

33 T. Giovannini, L. Bonatti, P. Lafiosca, L. Nicoli, M. Castagnola, P. G. Illobre, S. Corni and C. Cappelli, Do We Really Need Quantum Mechanics to Describe Plasmonic Properties of Metal Nanostructures?, *ACS Photonics*, 2022, **9**, 3025–3034.

34 P. Lafiosca, L. Nicoli, L. Bonatti, T. Giovannini, S. Corni and C. Cappelli, QM/Classical Modeling of Surface Enhanced Raman Scattering Based on Atomistic Electromagnetic Models, *J. Chem. Theory Comput.*, 2023, **19**, 3616–3633.

35 T. Giovannini, M. Rosa, S. Corni and C. Cappelli, A classical picture of subnanometer junctions: an atomistic Drude approach to nanoplasmonics, *Nanoscale*, 2019, **11**, 6004–6015.

36 L. Bonatti, G. Gil, T. Giovannini, S. Corni and C. Cappelli, Plasmonic resonances of metal nanoparticles: atomistic vs. Continuum approaches, *Front. Chem.*, 2020, **8**, 340.

37 P. Lafiosca, T. Giovannini, M. Benzi and C. Cappelli, Going Beyond the Limits of Classical Atomistic Modeling of Plasmonic Nanostructures, *J. Phys. Chem. C*, 2021, **125**, 23848–23863.

38 T. Giovannini, L. Bonatti, M. Polini and C. Cappelli, Graphene plasmonics: Fully atomistic approach for realistic structures, *J. Phys. Chem. Lett.*, 2020, **11**, 7595–7602.

39 L. Bonatti, L. Nicoli, T. Giovannini and C. Cappelli, In silico design of graphene plasmonic hot-spots, *Nanoscale Adv.*, 2022, **4**, 2294–2302.
40 S. Zanotto, L. Bonatti, M. F. Pantano, V. Mišeikis, G. Speranza, T. Giovannini, C. Coletti, C. Cappelli, A. Tredicucci and A. Toncelli, Strain-Induced Plasmon Confinement in Polycrystalline Graphene, *ACS Photonics*, 2023, **10**, 394–400.
41 L. Nicoli, P. Lafiosca, P. Grobas Illobre, L. Bonatti, T. Giovannini and C. Cappelli, Fully atomistic modeling of plasmonic bimetallic nanoparticles: nanoalloys and core-shell systems, *Front. Photon.*, 2023, **4**, 2673–6853.
42 S. Corni and J. Tomasi, Excitation energies of a molecule close to a metal surface, *J. Chem. Phys.*, 2002, **117**, 7266–7278.
43 S. Corni and J. Tomasi, Lifetimes of electronic excited states of a molecule close to a metal surface, *J. Chem. Phys.*, 2003, **118**, 6481–6494.
44 O. Andreussi, S. Corni, B. Mennucci and J. Tomasi, Radiative and nonradiative decay rates of a molecule close to a metal particle of complex shape, *J. Chem. Phys.*, 2004, **121**, 10190–10202.
45 M. Caricato, O. Andreussi and S. Corni, Semiempirical (ZINDO-PCM) Approach to Predict the Radiative and Nonradiative Decay Rates of a Molecule Close to Metal Particles, *J. Phys. Chem. B*, 2006, **110**, 16652–16659.
46 A. Pinchuk, G. Von Plessen and U. Kreibig, Influence of interband electronic transitions on the optical absorption in metallic nanoparticles, *J. Phys. D: Appl. Phys.*, 2004, **37**, 3133.
47 A. Pinchuk, U. Kreibig and A. Hilger, Optical properties of metallic nanoparticles: influence of interface effects and interband transitions, *Surf. Sci.*, 2004, **557**, 269–280.
48 B. Balamurugan and T. Maruyama, Evidence of an enhanced interband absorption in Au nanoparticles: size-dependent electronic structure and optical properties, *Appl. Phys. Lett.*, 2005, **87**, 143105.
49 A. Liebsch, Surface-plasmon dispersion and size dependence of Mie resonance: silver versus simple metals, *Phys. Rev. B*, 1993, **48**, 11317.
50 T. Giovannini, A. Puglisi, M. Ambrosetti and C. Cappelli, Polarizable QM/MM approach with fluctuating charges and fluctuating dipoles: the QM/FQFμ model, *J. Chem. Theory Comput.*, 2019, **15**, 2233–2245.
51 A. Dreuw and M. Head-Gordon, Single-Reference ab Initio Methods for the Calculation of Excited States of Large Molecules, *Chem. Rev.*, 2005, **105**, 4009–4037.
52 A. H. Larsen, *et al.*, The atomic simulation environment—a Python library for working with atoms, *J. Phys.: Condens.Matter*, 2017, **29**, 273002.
53 M. Barbry, P. Koval, F. Marchesin, R. Esteban, A. Borisov, J. Aizpurua and D. Sánchez-Portal, Atomistic near-field nanoplasmonics: reaching atomic-scale resolution in nanooptics, *Nano Lett.*, 2015, **15**, 3410–3419.
54 X. Chen and L. Jensen, Morphology dependent near-field response in atomistic plasmonic nanocavities, *Nanoscale*, 2018, **10**, 11410–11417.
55 U. Kreibig and M. Vollmer, *Optical properties of metal clusters*, Springer Science & Business Media, 2013, vol. 25.
56 C. Novo, D. Gomez, J. Perez-Juste, Z. Zhang, H. Petrova, M. Reismann, P. Mulvaney and G. V. Hartland, Contributions from radiation damping and surface scattering to the linewidth of the longitudinal plasmon band of gold nanorods: a single particle study, *Phys. Chem. Chem. Phys.*, 2006, **8**, 3540–3546.
57 V. Juvé, M. F. Cardinal, A. Lombardi, A. Crut, P. Maioli, J. Pérez-Juste, L. M. Liz-Marzán, N. Del Fatti and F. Vallée, Size-dependent surface plasmon resonance broadening in nonspherical nanoparticles: single gold nanorods, *Nano Lett.*, 2013, **13**, 2234–2240.
58 B. Foerster, A. Joplin, K. Kaefer, S. Celiksoy, S. Link and C. Sönnichsen, Chemical interface damping depends on electrons reaching the surface, *ACS Nano*, 2017, **11**, 2886–2893.
59 O. A. Douglas-Gallardo, G. J. Soldano, M. M. Mariscal and C. G. Sánchez, Effects of oxidation on the plasmonic properties of aluminum nanoclusters, *Nanoscale*, 2017, **9**, 17471–17480.
60 C. Geuzaine and J.-F. G. Remacle, A 3-D finite element mesh generator with built-in pre- and post-processing facilities, *Int. J. Numer. Methods Eng.*, 2009, **79**, 1309–1331.
61 S. Corni and J. Tomasi, Surface enhanced Raman scattering from a single molecule adsorbed on a metal particle aggregate: A theoretical study, *J. Chem. Phys.*, 2002, **116**, 1156–1164.
62 R. Cammi and J. Tomasi, Remarks on the use of the apparent surface charges (ASC) methods in solvation problems: Iterative versus matrix-inversion procedures and the renormalization of the apparent charges, *J. Comput. Chem.*, 1995, **16**, 1449–1458.
63 J. Tomasi, B. Mennucci and R. Cammi, Quantum Mechanical Continuum Solvation Models, *Chem. Rev.*, 2005, **105**, 2999–3094.
64 P. G. Etchegoin, E. Le Ru and M. Meyer, An analytic model for the optical properties of gold, *J. Chem. Phys.*, 2006, **125**, 164705.
65 M. G. Blaber, A.-I. Henry, J. M. Bingham, G. C. Schatz and R. P. Van Duyne, LSPR Imaging of Silver Triangular Nanoprisms: Correlating Scattering with Structure Using Electrodynamics for Plasmon Lifetime Analysis, *J. Phys. Chem. C*, 2012, **116**, 393–403.
66 P. B. Johnson and R.-W. Christy, Optical constants of the noble metals, *Phys. Rev. B*, 1972, **6**, 4370.
67 E. Baerends, *et al.*, *ADF (Version 2020.X); Theoretical Chemistry*, Vrije Universiteit, Amsterdam, The Netherlands, 2020, **http://www.scm.com**.
68 E. Dulkeith, M. Ringler, T. A. Klar, J. Feldmann, A. Muñoz Javier and W. J. Parak, Gold Nanoparticles Quench Fluorescence by Phase Induced Radiative Rate Suppression, *Nano Lett.*, 2005, **5**, 585–589.
69 P. Reineck, D. Gómez, S. H. Ng, M. Karg, T. Bell, P. Mulvaney and U. Bach, Distance and Wavelength Dependent Quenching of Molecular Fluorescence by Au@SiO2 Core–Shell Nanoparticles, *ACS Nano*, 2013, **7**, 6636–6648.

70 J. D. Pajović, R. J. Dojčilović, S. Kaščáková, M. Réfrégiers, D. K. Božanić and V. Djoković, Enhanced resonance energy transfer in gold nanoparticles bifunctionalized by tryptophan and riboflavin and its application in fluorescence bioimaging, *Colloids Surf., B*, 2023, **227**, 113340.
71 A. Trügler, *Optical Properties of Metallic Nanoparticles*, Springer International Publishing, 2016.
72 P. Anger, P. Bharadwaj and L. Novotny, Enhancement and Quenching of Single-Molecule Fluorescence, *Phys. Rev. Lett.*, 2006, **96**, 113002.
73 H. Yuan, S. Khatua, P. Zijlstra, M. Yorulmaz and M. Orrit, Thousand-fold Enhancement of Single-Molecule Fluorescence Near a Single Gold Nanorod, *Angew. Chem., Int. Ed.*, 2013, **52**, 1217–1221.
74 E. Wientjes, J. Renger, A. G. Curto, R. Cogdell and N. F. van Hulst, Strong antenna-enhanced fluorescence of a single light-harvesting complex shows photon antibunching, *Nat. Commun.*, 2014, **5**, 4236.
75 Z. Mei and L. Tang, Surface-Plasmon-Coupled Fluorescence Enhancement Based on Ordered Gold Nanorod Array Biochip for Ultrasensitive DNA Analysis, *Anal. Chem.*, 2017, **89**, 633–639.
76 J.-F. Li, C.-Y. Li and R. F. Aroca, Plasmon-enhanced fluorescence spectroscopy, *Chem. Soc. Rev.*, 2017, **46**, 3962–3979.
77 A. Rosławska, T. c. v. Neuman, B. Doppagne, A. G. Borisov, M. Romeo, F. Scheurer, J. Aizpurua and G. Schull, Mapping Lamb, Stark, and Purcell Effects at a Chromophore-Picocavity Junction with Hyper-Resolved Fluorescence Microscopy, *Phys. Rev. X*, 2022, **12**, 011012.
78 J. Doležal, A. Sagwal, R. C. de Campos Ferreira and M. Švec, Single-Molecule Time-Resolved Spectroscopy in a Tunable STM Nanocavity, *Nano Lett.*, 2024, **24**, 1629–1634.